Development of a thermopile infrared sensor using stacked double polycrystalline silicon layers based on the CMOS process

2013 J. Micromech. Microeng. 23 065026

(http://iopscience.iop.org/0960-1317/23/6/065026)

J. Micromech. Microeng. **23** (2013) 065026 (14pp) doi:10.1088/0960-1317/23/6/065026

Development of a thermopile infrared sensor using stacked double polycrystalline silicon layers based on the CMOS process

Huchuan Zhou[1,2], **P Kropelnicki**[2], **J M Tsai**[2] **and Chengkuo Lee**[1,3]

[1] Department of Electrical and Computer Engineering, National University of Singapore, 4 Engineering Drive 3, Singapore 117576, Singapore
[2] Institute of Microelectronics, A*STAR 11 Science Park Road, Science Park II, Singapore 117685, Singapore

E-mail: elelc@nus.edu.sg

Received 18 October 2012, in final form 14 March 2013
Published 13 May 2013
Online at stacks.iop.org/JMM/23/065026

Abstract
A stacked double-layer (SDL) thermopile-based infrared sensor, which comprised of 96 thermocouples on a suspended membrane, has been designed and fabricated with a CMOS-compatible process. The thermoelectric properties were characterized, and responsivity (R_s) of 202.8 V W^{-1} and detectivity (D^*) of 2.85*10^8 cm Hz$^{1/2}$ W^{-1} for a SDL thermopile were derived.

(Some figures may appear in colour only in the online journal)

1. Introduction

Nowadays, more and more microelectromechanical systems (MEMS) based on the complementary metal–oxide semiconductor (CMOS)-compatible process are developed for various applications, due to the inherent advantages of the CMOS-compatible process, including small dimensions, light weight, fast response and integrated circuits (ICs) for further signal processing [1, 2]. One of the representative CMOS MEMS devices is the thermopile [3–8]. A thermopile is a set of serialy connected thermoelectric strip pairs where the Seebeck coefficient is different for materials forming the pair. Due to the Seebeck effect, thermoelectric voltage is generated linearly corresponding to the temperature difference between the hot-junction and the cold-junction of the thermopile structure [7–10].

Thermopiles in the format of single detector have been used as non-contact temperature sensors, flow sensors, gas sensors, accelerometers and AC–DC converters, while thermopile array devices have been demonstrated as infrared (IR) imaging devices and microspectrometers [11–23].

Among the reported thermoelectric materials used in thermopiles, Bi_2Te_3 and Sb_2Te_3 are the well-known n-type and p-type materials which generate the highest figure-of-merit, i.e. zT, within 200 °C [24, 25]. However, these materials are not CMOS-compatible materials. Thus they cannot be fabricated in standard CMOS manufacturing lines [26]. Although some more accessible thin film metal materials, e.g. nickel and chromium, are also used in thermopiles, their low Seebeck coefficient limits the performance of thermopiles [27, 28]. Recently semiconductor-based thermopiles were presented using germanium (Ge), silicon carbide (SiC) and polycrystalline silicon (poly-Si) which could be made by the CMOS-compatible fabrication process [29, 30]. In this paper, n/p doped poly-Si are used as thermopile materials due to its low cost production and sound Seebeck coefficient even at high temperatures, compared to germanium (Ge) and silicon carbide (SiC). Xie *et al* conducted a detailed study on the zT of boron- and phosphorus-doped low-pressure chemical vapor deposition (LPCVD) poly-Si as the thermopile materials [31, 32], showing the optimized zT with respect to doping concentration of poly-Si at room temperature. The conventional CMOS-based thermopiles using n-doped and p-doped poly-Si strip patterns are typically fabricated on the

[3] Author to whom any correspondence should be addressed.

same layer [4, 22, 26], and are termed as coplanar thermopile. It is not the most efficient way to arrange and integrate a pair of n/p-doped poly-Si for thermopile applications. In this paper, we developed a new thermopile structure having two vertically integrated n/p-doped poly-Si layers to reduce the footprint and surface area exposed to air.

The selection of a mechanically supporting material for the thermopile is also crucial. The supporting material should have high thermal resistance (or low thermal conductance), high mechanical and thermal stability. Polymers, e.g. SU-8, are emerging as attractive materials for this purpose [33–35], due to their relative low thermal conductance, flexibility [36] and potential on integration as a biocompatible layer for bio-chips [37]. We focus on CMOS materials in this paper, therefore silicon-di-oxide (SiO_2) was used as the supporting material, because of its low thermal conductance and high thermal and mechanical stability [38, 39]. The contradiction between thermal resistance and electrical resistance of the thermopile is always a design tradeoff [40, 41]. In order to reach high responsivity, thermal resistance and electrical resistance should be optimized together, while the surface area of thermopile has to be incorporated into the design optimization, as it will affect the overall thermal conductance due to the dependence of heat loss from thermopile to air.

In this paper, we propose a new design of CMOS-compatible and poly-Si-based thermopile using stacked double-layer (SDL) [42] structures. The electrical resistivity, electrical specific contact resistivity, thermal conductivity and Seebeck coefficient of the materials are characterized. Furthermore, the comparison between the performance of the conventional coplanar thermopile and the SDL thermopile is conducted to show the advantages of the SDL. Finally, the dependence of responsivity under ambient pressure is reported.

2. Design and optimization

2.1. Theory of thermopile

The thermopile consists of many thermocouple pairs which are electrically connected in series. A thermocouple comprises of a pair of materials with different Seebeck coefficients. According to the Seebeck effect, thermoelectric power is generated when there is a temperature difference between the two ends. The output voltage of a single thermocouple $V_{\text{out-single}}$ can be described mathematically as [42]

$$V_{\text{out-single}} = \Delta T(\alpha_1 - \alpha_2) = \Delta T\alpha_{12}, \tag{1}$$

where ΔT is the temperature difference between the two ends of the thermocouple. The end which has a higher temperature is known as the 'hot-junction', while the other end is known as the 'cold-junction'. α_1 and α_2 are the Seebeck coefficients of the two materials, and the difference between α_1 and α_2 is defined as α_{12}. In an infrared radiation sensor which uses a thermopile design, the hot-junction is the end close to the radiation absorber, while the cold-junction is the end connected to a heat sink, e.g. the single crystal silicon substrate, which represents ambient temperature. The absorber layer absorbs infrared radiation from the IR source and converts radiation power into heat, which causes the temperature rise in the hot-junction. In our experiment, the hot-junction can also be connected to a microheater in order to create the desired temperature at the hot-junction in a controlled manner. Thus we can precisely calibrate the thermopile performance versus temperature difference built between hot-junction and cold-junction.

Due to the suspended thermopile structure, the hot-junction and cold-junction are thermally isolated. Thermal isolation leads to a relatively high temperature difference between these two junctions. Due to the Seebeck effect, as discussed above, the thermopile will generate an output voltage without any applied voltage bias. The thermopile is an array of thermocouples so the output voltage of the thermopile is

$$V_{\text{out}} = NV_{\text{out\_single}} = N\Delta T\alpha_{12}, \tag{2}$$

where N is the number of thermocouples.

The responsivity R_s can be expressed as

$$R_s = \frac{V_{\text{out}}}{P_{\text{absorb}}}, \tag{3}$$

where P_{absorb} is the infrared power that is absorbed by the thermopile and can be calculated as

$$P_{\text{absorb}} = \eta\varphi_0 A, \tag{4}$$

where η is the absorption rate of the absorber, φ_0 is the infrared radiation power density and A is the area of absorber.

According to the Stefan–Boltzmann law, the radiance power density from the source to the thermopile can be expressed as

$$\varphi_0 = \sigma\left(T_s^4 - T_0^4\right)A_s/(\pi l^2), \tag{5}$$

where σ is the Stefan–Boltzmann constant, T_s is the temperature of source, T_0 is ambient temperature, A_s is area of source and l is the distance between source and thermopile.

The field view is 2θ so we can replace A_s with the detectable target area A_s', which is smaller than A_s.

$$\mathrm{A}_s' = \pi \mathrm{l}^2 \sin^2\theta. \tag{6}$$

By substituting (6) into (5), φ_0 can be derived as

$$\varphi_0 = \sigma\left(T_s^4 - T_0^4\right)\sin^2\theta, \tag{7}$$

and

$$P_{\text{absorb}} = \eta\sigma\left(T_s^4 - T_0^4\right)\sin^2\theta A. \tag{8}$$

Then we can calculate the responsivity as [43]

$$R_s = \frac{N\Delta T\alpha_{12}}{\eta\sigma\left(T_s^4 - T_0^4\right)\sin^2\theta A}, \tag{9}$$

where ΔT is the temperature difference between the cold-junction and hot-junction. The ΔT can be calculated by [44]

$$\Delta T = P_{\text{absorb}} * R_{\text{ther}} = \eta\varphi_0 A R_{\text{ther}}, \tag{10}$$

where R_{ther} is the thermal resistance.

The thermal resistance consists of three parts: K_s, K_g and K_r, which are the thermal conductance of the structure, atmosphere and radiation, respectively:

$$R_{\text{ther}} = \frac{1}{K_s + K_g + K_r}. \tag{11}$$

The thermal conductance of the structure is expressed by

$$K_s = \sum \frac{k_i t_i w_i}{l_i}, \tag{12}$$

where the k_i, t_i, w_i, l_i, are the thermal conductivity, thickness, width and length of each part.

The thermal conductance of the atmosphere is expressed by equation (13)

$$K_g = w_{SiO_2} l_{SiO_2} k_g \left(\frac{1}{d_1} + \frac{1}{d_2}\right), \tag{13}$$

where w_{SiO2} and l_{SiO2} are the width and length of the SiO_2 dielectric membrane (respectively), k_g is the thermal conductance of the atmosphere, d_1 is the distance between the membrane and the bottom of the release cavity, d_2 is the distance between the top of the sensor and the cover of the package. The cross-talk through air has been studied carefully by other researchers [45, 46].

Assuming $T \ll T_0$, the thermal conductance due the radiation is expressed by

$$K_r = 4 w_{SiO_2} l_{SiO_2} \xi \sigma T_0^3, \tag{14}$$

where ξ is the emissivity of the thermopile.

Another important parameter is the detectivity, D^*, which is expressed as

$$D^* = \sqrt{A\Delta f}/\mathrm{NEP}, \tag{15}$$

where Δf is the frequency bandwidth of the read out system, NEP is the noise equivalent power that can be expressed as

$$\mathrm{NEP} = V_n/R_s \tag{16}$$

where V_n is the equivalent noise voltage. We can assume that all the noise is Johnson noise which is caused by the resistance of thermopile:

$$V_n = \sqrt{4kTR\Delta f}, \tag{17}$$

where k is Boltzmann constant, T is the temperature of thermopile (in kelvin). Then we can calculate the detectivity as

$$D^* = R_s\sqrt{A/4kTR}. \tag{18}$$

The responsivity, R_s, detectivity, D^*, and the noise equivalent power, NEP, are the main parameters used to characterize the thermopile. R_s stands for the output of the thermopile which corresponds to the output efficiency of the sensor. NEP represents the input power when the output voltage is equal to the noise power. D^* is inverse of NEP and is normalized by the absorption area and signal frequency. The NEP indicates the value of signal which can be detected by the sensor.

2.2. Design of thermopile

As described in section 2.1, the possibility of achieving a highly effective thermoelectric sensor lies in two important parts: relatively low thermal conductance and high difference in Seebeck coefficients (α_{12}) between the two materials which form the thermocouple. Conventional coplanar thermopiles have drawbacks in these two points. In order to avoid these drawbacks, we suggest a stacked double-layer (SDL) thermopile.

Table 1. Material properties used for thermopile design.

	n-type poly-Si	p-type poly-Si	Al	SiO_2	Si
Thermal conductivity (W mK^{-1})	29.7	28.4	237	1.25	149
Seebeck coefficient (μV K^{-1})	−110	130	−1.8	–	–
Resistivity ($\mu\Omega$ m)	8.9	13.7	0.03	–	–

Figure 1 shows the schematic drawing of the conventional coplanar thermopile and the SDL thermopile. The thermopiles are formed in a 'plus' shaped structure in which the central part forms an absorber which absorbs the infrared radiation causing a temperature rise at the hot-junction. The whole thermopile is suspended on a thin membrane so that the heat can transfer from the hot-junction, only through the thermopile to the cold-junction, which is thermally connected to the single crystalline silicon substrate (heat sink), as shown in figure 1. The silicon substrate has high thermal conductance and large thermal mass to maintain a relatively constant temperature at the cold-junction. As a result, there will be temperature difference between the hot and cold-junctions, inducing a voltage drop between these two junctions.

The poly-Si strips are interconnected by Al lines in series thus the thermopile might suffer from the problem of high contact resistance between Al and poly-Si [26], causing a high Johnson noise which might decrease the device performance. Hence, the process condition was optimized to increase the surface doping concentration through high doping dose and low implantation energy, which significantly reduced the contact resistance between Al and poly-Si [47].

Figure 2 shows the comparison between one single thermocouple in the conventional coplanar thermopile and SDL thermopile, respectively. The coplanar thermopile utilizes doped poly-Si and Al as thermocouple, while the thermocouples in the SDL thermopile are formed by a pair of n-type poly-Si and p-type poly-Si. It is the difference of the properties of Al and doped poly-Si that makes a huge difference in the performance of the conventional coplanar thermopile and the SDL thermopile. Details of the material properties that are used in the thermopile design are shown in table 1. Both n and p-type poly-Si are studied in this work. Table 1 indicates that the absolute value of the Seebeck coefficient of Al is much lower than the doped poly-Si, while the thermal conductance of Al is much higher than that of the poly-Si. As shown in equations (1) and (9), a low Seebeck coefficient and high thermal conductance (low thermal resistance) will both lower the performance of the thermopile. In the conventional coplanar thermopile, metal lines are used for connection of the hot and cold-junctions. With such structure, a large amount of heat will be transferred through the metal line from the hot-junction to the cold-junction, which causes a smaller temperature difference between them, and so a smaller output voltage.

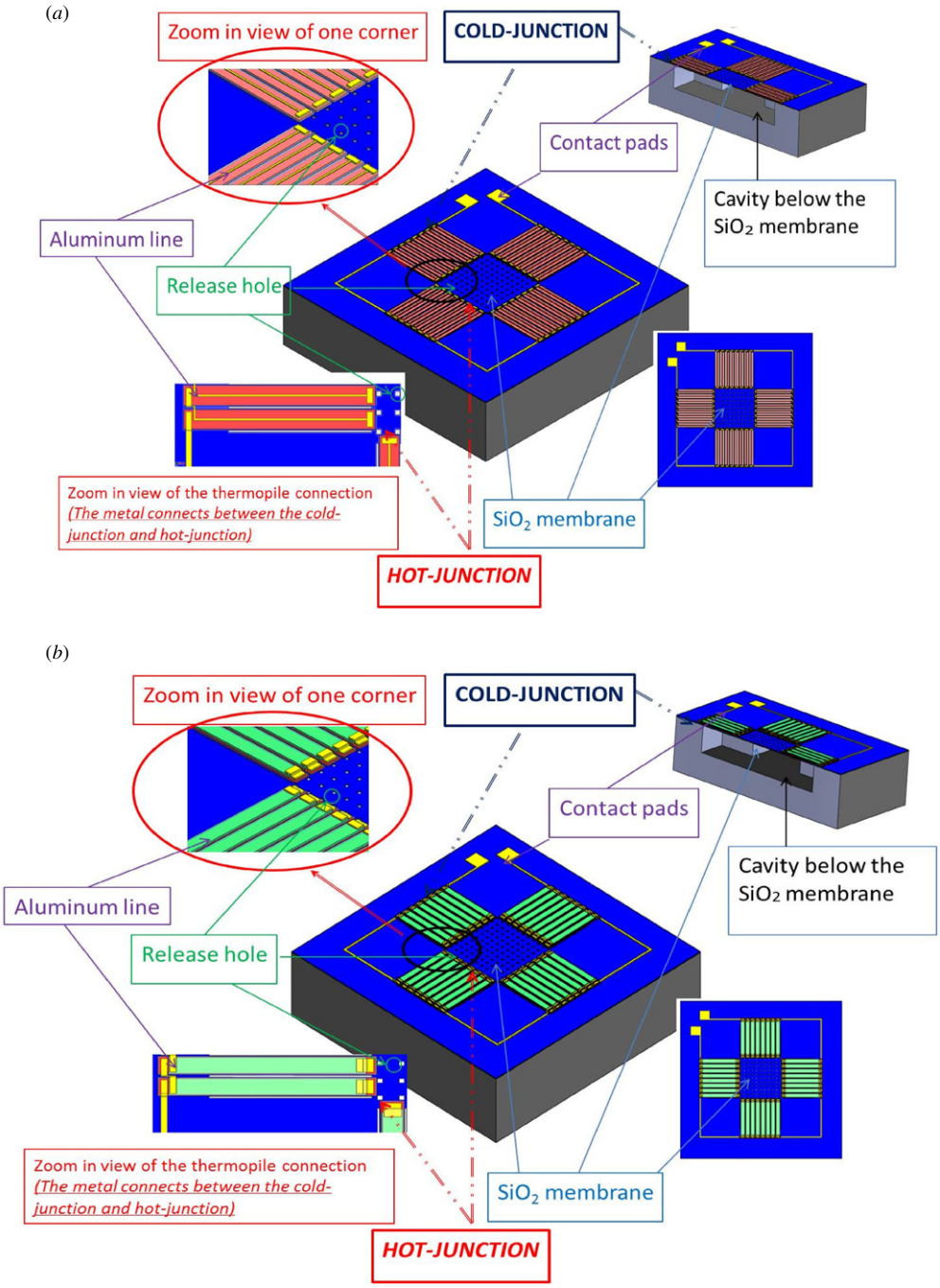

Figure 1. Schematic diagram of the (*a*) conventional coplanar thermopile and (*b*) vertically integrated SDL thermopile.

However, the stacked thermopile does not have such disadvantages. The Al acts as a connector between the n-type and p-type silicon, so that the heat between the hot and cold-junction is only transferred through the doped silicon (figure 2). Although the thickness of poly-Si in this design is twice that of the planar structure, the thermal conductance between the hot-junction and cold-junction is lower because of the relatively low thermal conductivity of poly-Si compared to Al.

The SDL thermopile also has advantage in the aspect of the Seebeck coefficient difference, α_{12}. α_{12} of the thermocouple formed by a doped poly-Si and Al (shown in the left of figure 2) is only half of the one formed by a pair of n-type poly-Si and p-type poly-Si (shown in the right of figure 2). Hence the output voltage of the SDL thermopile will also be higher according to equation (2).

Although the SDL thermopile has advantages in the thermal conductance and the Seebeck Coefficient difference, there is still a drawback in the electric conductance. As shown in table 1, the electrical resistivity of polysilicon is higher than that of Al, which means that the electrical resistance of the SDL thermopile is almost double of that of a conventional coplanar thermopile if we omit the contact resistance. The electrical resistivity, as shown in equation (17), affects the noise. Therefore, the noise will increase at most to $\sqrt{2}$.

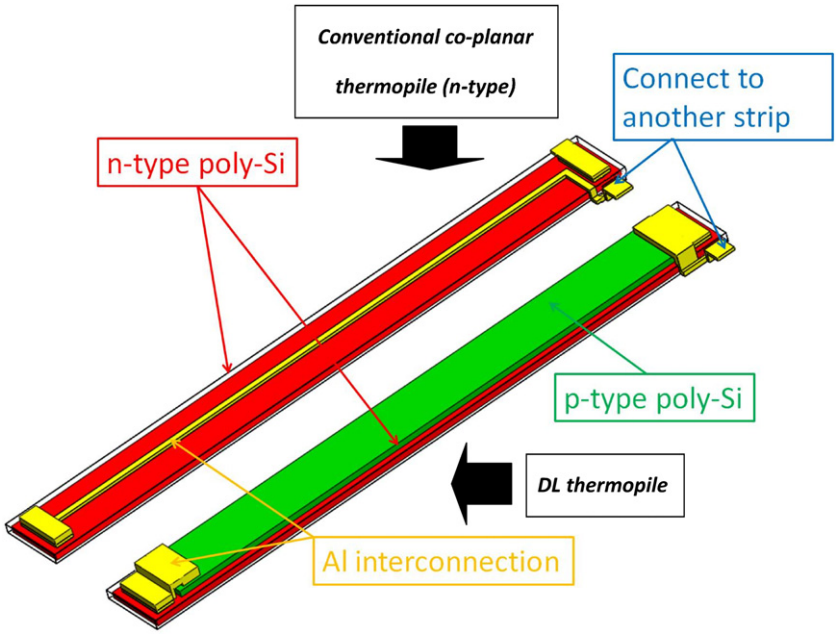

Figure 2. Comparison between a single thermocouple in the conventional coplanar thermopile and SDL thermopile.

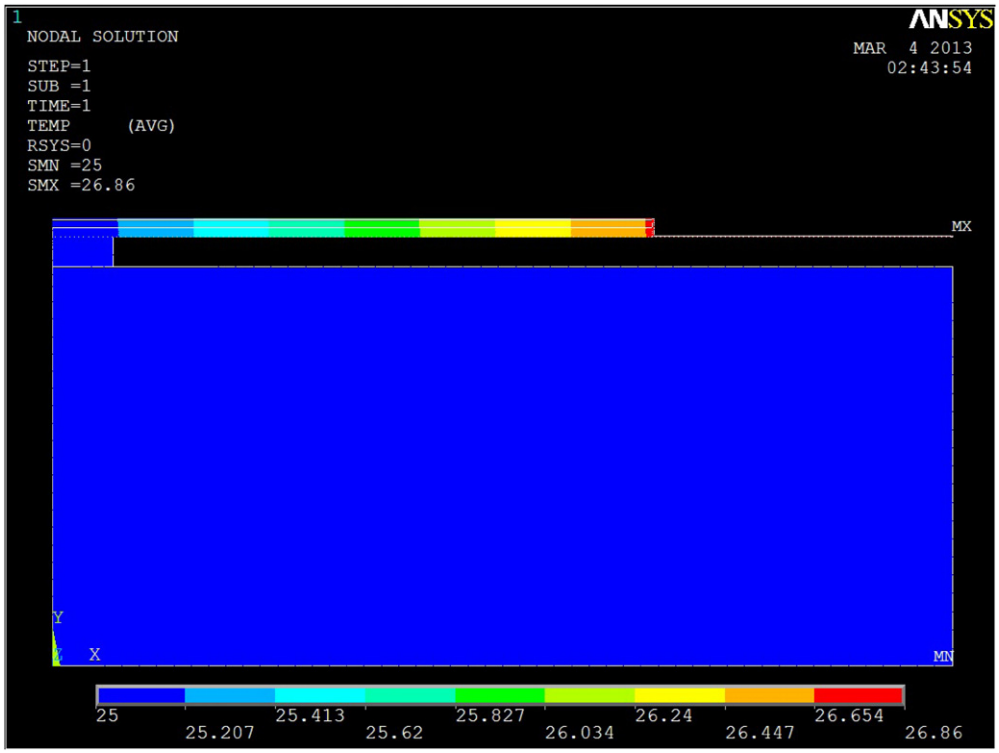

Figure 3. 2D ANSYS simulation result showing the cross-sectional view of the temperature difference in the thermopile.

However, according to the discussion above, the R_s of the SDL thermopile will at least be double of that of a conventional coplanar thermopile, which means that D^* will also increase, according to equation (17). In summary, the performance of the SDL thermopile is better from an overall point of view.

Optimization of the dimension parameters were conducted with ANSYS-12.0 finite element simulation software and MATLAB 7.0. To get the temperature difference between the hot-junction and cold-junction of the thermopile, the simulation was done in a 2D manner as the thermopile design is symmetrical. An example of the simulation result is shown in figure 3. Using the derived temperature difference data obtained from simulation, the R_s and D^* values were calculated using MATLAB based on the equations presented above and evaluation of the performance of the thermopiles with different dimensions were made. The optimal result is obtained when the length of the thermopile equals to 600 μm, the width of the thermopile equals to 12 μm and

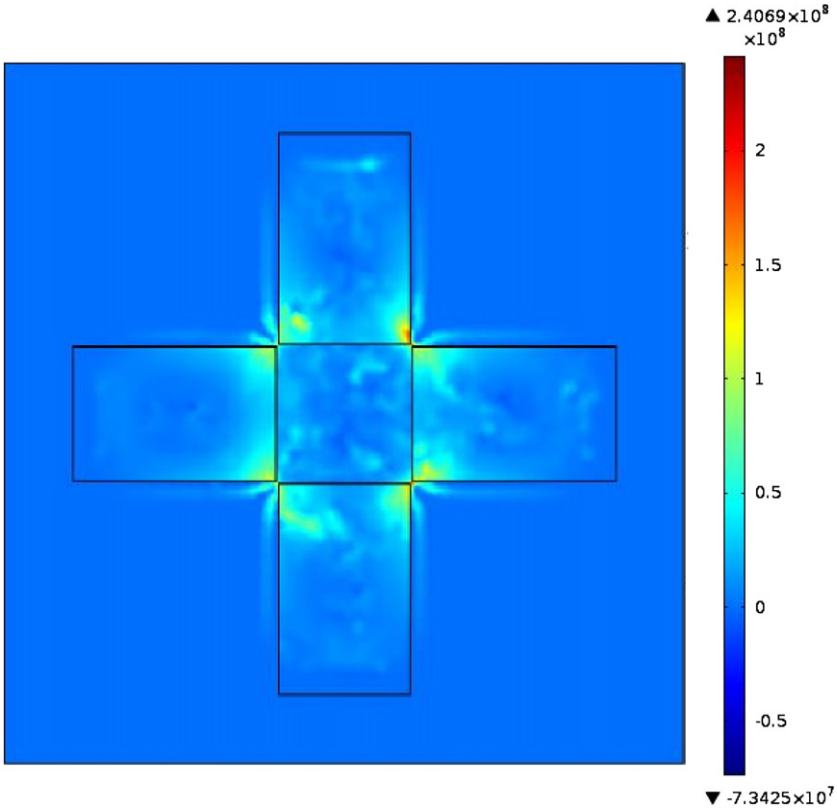

Figure 4. 3D COMSOL simulation result showing the stress distribution on the thermopile with the load of 10 atmospheric pressure.

the number of thermocomples equals to 96. The thickness of the poly-Si strips are 0.7 μm and the thickness of the SiO_2 electrical isolation layer is 0.15 μm. Based on these parameters, the simulation was conducted and the results show that the responsivity of n-type planar thermopile is 37.08 V W^{-1} and the detectivity is $0.93*10^8$ cm $Hz^{1/2}$ W^{-1} while the responsivity of SDL thermopile is 76.9 V W^{-1}, detectivity is $1.53*10^8$ cm $Hz^{1/2}$ W^{-1}. Although in the simulation all properties of the materials, such as electric resistivity, thermal conductivity and Seebeck coefficient, are estimated value, it can still give us significant insights and hints for future designs.

Since the membrane is so large and the thickness is less than 2 μm, the mechanical stability needs to be studied. In order to study the mechanical stability, a simulation with COMSOL 4.3 has been conducted. The simulation result is shown in figure 4. The figure shows that the largest stress in the membrane is 240 MPa under 10% atmospheric pressure, less than the fracture strength 364 $\pm$ 57 MPa [48]. It is clear that the mechanical stability of the structure is quite good.

3. Fabrication and characterization

3.1. Fabrication of the thermopile

Figure 5 shows the CMOS-compatible microfabrication process flow of the SDL thermopiles reported in this paper. An 8″ silicon wafer with 725 μm thickness was used as the starting material. First, a 0.2 μm thick thermal insulating SiO_2 layer was deposited on the front side of the wafer by low-pressure chemical vapor deposition (LPCVD) at 600 °C as electrical isolation and mechanical supporting layer (figure 5(*a*)). Then, the 0.7 μm thick poly-Si as a thermoelectric layer was deposited at 580 °C in a furnace by LPCVD. The poly-Si layer was implanted with phosphorus at 120 keV energy and patterned by reactive ion etching (RIE) to form n-type thermoelectric strips with pattern dimension of 12 μm in width and 600 μm in length (figure 5(*b*)). 0.15 μm thick SiO_2, which serves as electrical insulation, was further deposited by plasma-enhanced chemical vapor deposition (PECVD) (figure 5(*c*)). A second poly-Si layer was deposited by LPCVD again, and it was boron implanted using 50 keV, then patterned to form the p-type thermoelectric strips. Subsequently a 0.15 μm SiO_2 was further deposited by PECVD as an electrical insulation layer (figure 5(*d*)). Doping dose of 10^{15} cm^{-2} was used in both implantation steps.

After the step of contact-via-opening for n-type poly-Si strips, n++ heavy doping was done with 40 KeV at contact via region. Following that contact-via-opening for p-type poly-Si strips was conducted, and subsequently a p++ contact via doping was done with 20 KeV. A doping dose of 10^{16} cm^{-2} was used in both cases. An annealing step was conducted at 1000 °C for 30 min (figure 5(*e*)). Then the Al layer was deposited by sputtering and patterned to form metal interconnection between n-type and p-type poly-Si strips (figure 5(*f*)). To establish a good ohmic contact between the Al and poly-Si, the wafer was annealed at 420 °C for 30 min. In order to confine the heat flux within the thermopile beams, the underneath silicon was etched to form a cavity, where the etching steps were conducted by depositing the 0.5 μm thick SiO_2 hard mask first (figure 5(*g*)) and the deep silicon trenches via deep reactive ion

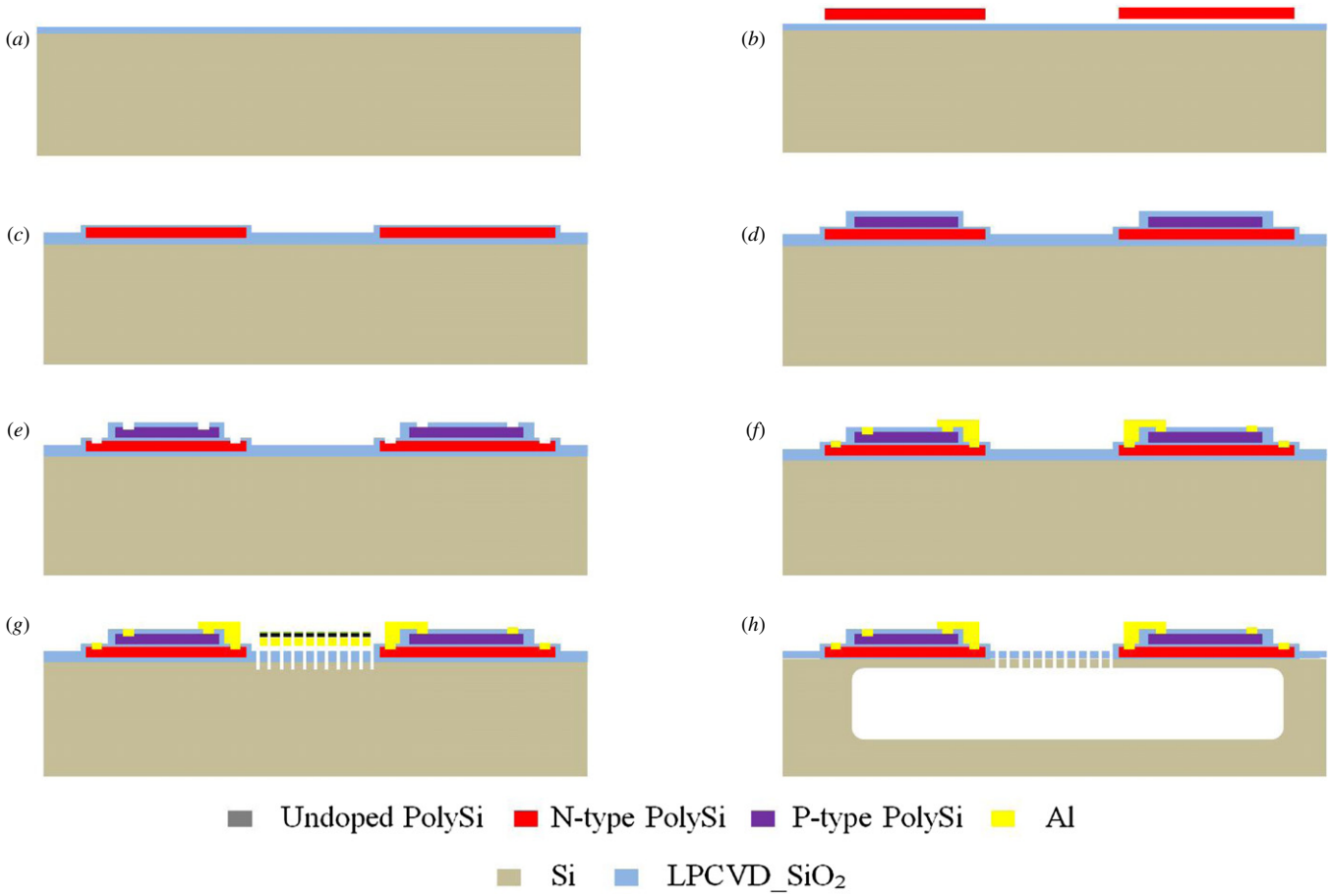

Figure 5. Fabrication process flow: (*a*) deposition of thermal SiO_2 on silicon wafer by LPCVD, (*b*) poly-Si deposition and n doping and definition by etching; fabrication of the micro-heater at the same time, (*c*) PECVD SiO_2 dielectric layer deposition, (*d*) poly-Si deposition and p doping and definition by etching, covered by PECVD SiO_2), (*e*) contact via open and contact doping, (*f*) Al wire and absorb layer deposition, (*g*) release hole opening, (*h*) front-side release.

etching (DRIE) based on SF_6 and C_4F_8 gases was used until 10 μm etch depth and then the wafer is isotropically etched by SF_6 to remove the silicon trench structures (figure 5(*h*)).

3.2. Characterization of the properties of poly-Si

The electrical resistivity and specific contact resistivity between Al and poly-Si are both crucial to the design of thermopiles because these two parameters determine the NEP and D^*. As discussed in section 2.1, low electric resistivity and specific contact resistivity between Al and poly-Si are desired for better design of thermopile. In this paper, the resistivity was determined by the van-der-Pauw structure (figure 6(*a*)). The resistivities of n-type poly-Si and p-type poly-Si are 9.6 $\mu\Omega$ m and 15.9 $\mu\Omega$ m, respectively. The electric contact resistance was derived by the Kelvin structure (figure 6(*b*)) [47]. The specific contact resistivity of Al-to-n-type-poly-Si and Al-to-p-type-poly-Si are 10.4 $\mu\Omega$ cm^2 and 4.3 $\mu\Omega$ cm^2, which determines that the surface doping concentration are both around 10^{20} cm^{-3} [49].

The Seebeck coefficient and thermal conductance were determined by a cantilever test structure (figure 7), which comprises of three layers: thermal SiO_2, doped poly-Si and PECVD SiO_2. Because the theoretical thermal conductance

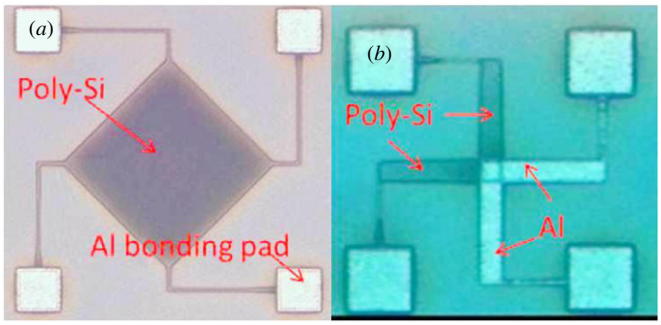

Figure 6. Test structure for resistivity and contact resistivity: (*a*) van-der-Pauw structure to measure the resistivity of the poly-Si, (*b*) Kelvin structure to test the contact resistivity.

of SiO_2 is much lower than the doped poly-Si this cantilever is appropriate for determining the thermal conductance of the poly-Si. The geometries of n-type and p-type cantilever test structure are the same and the only difference lies in the doping type of the poly-Si. The thickness of poly-Si in the test structure is 0.7 μm, which is the same as that of the thermopile sensor, while the width is 90 μm and the length is 300 μm. The width of the Al line is 1 μm. As the width of the poly-Si is much larger than the metal line, the impact of the thermal conductance of the metal line is minimized.

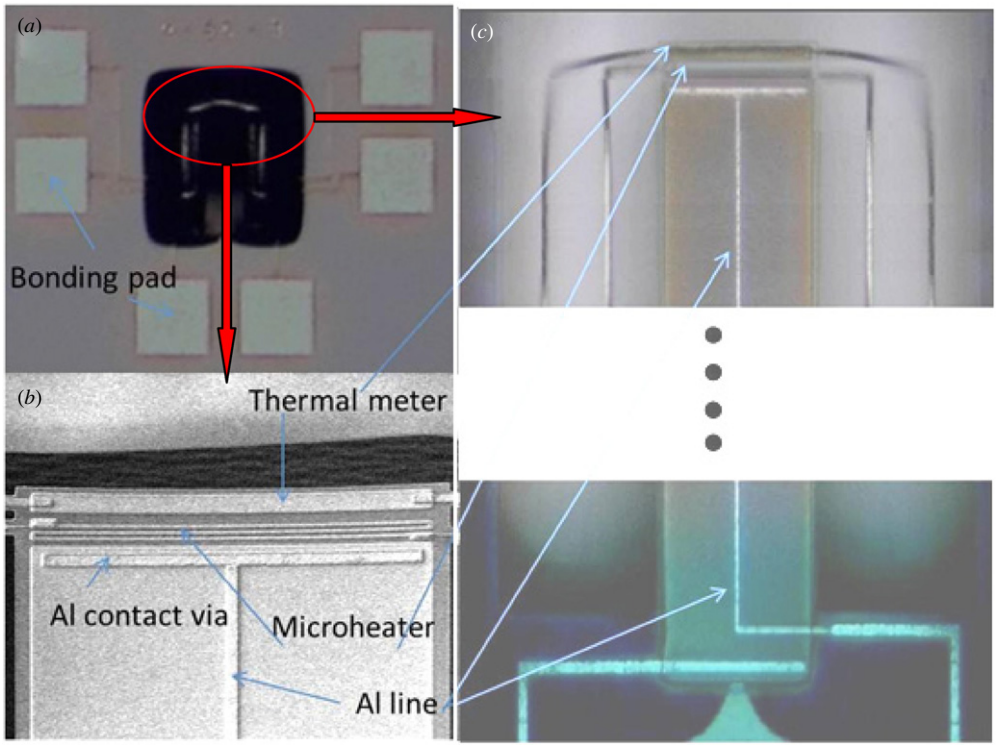

Figure 7. Optical microscope and SEM pictures of the test structure, (*a*) optical microscope figure of the overall test structure, (*b*) zoom-in SEM picture of the upside, (*c*) focused optical microscope pictures.

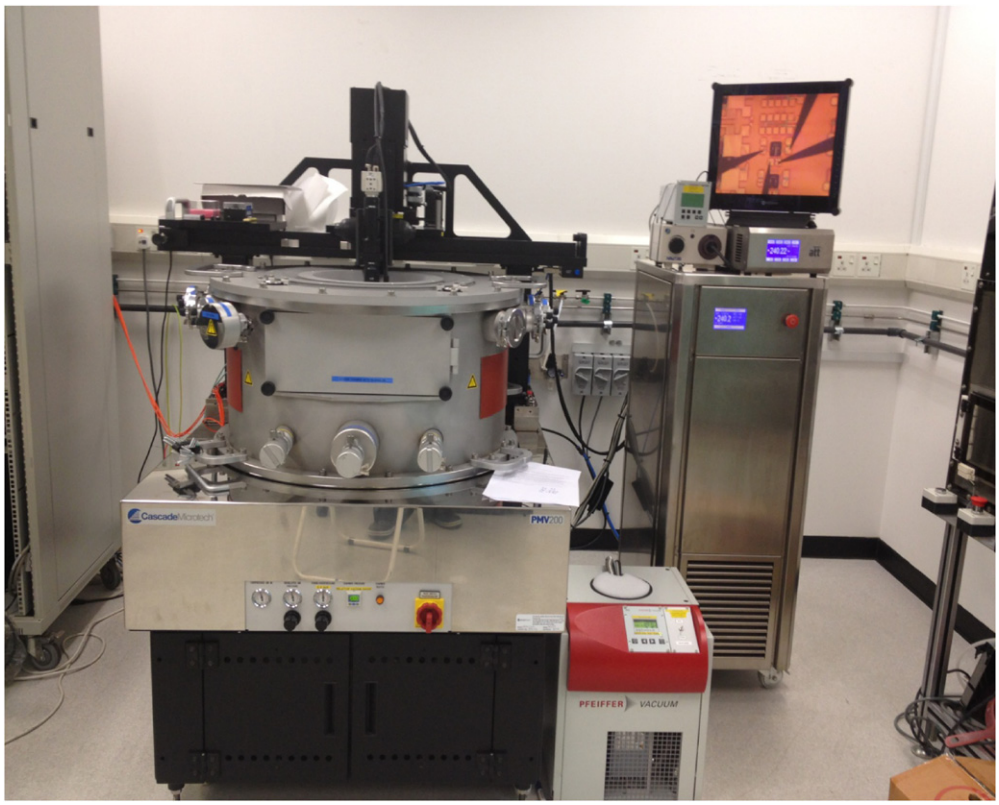

Figure 8. Equipment for testing.

The electrical measurement was carried out using a semiconductor parameter analyzer (Agilent technology, 4156C) equipped with a probe station (Cascade Microtech, PMV200) (figure 8).

Figure 9 shows the measurement results of the n-type cantilever test structure. In order to observe the thermocouple's performance, a bias voltage is applied from −5 V to 5 V in steps of 0.1 V. The hot-junction is connected to the ground, resulting

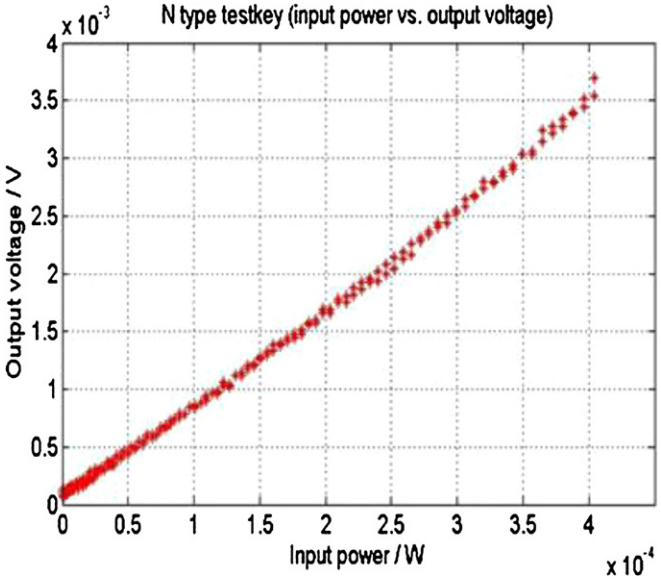

Figure 9. n-type thermopile test structure characterization input power versus output voltage.

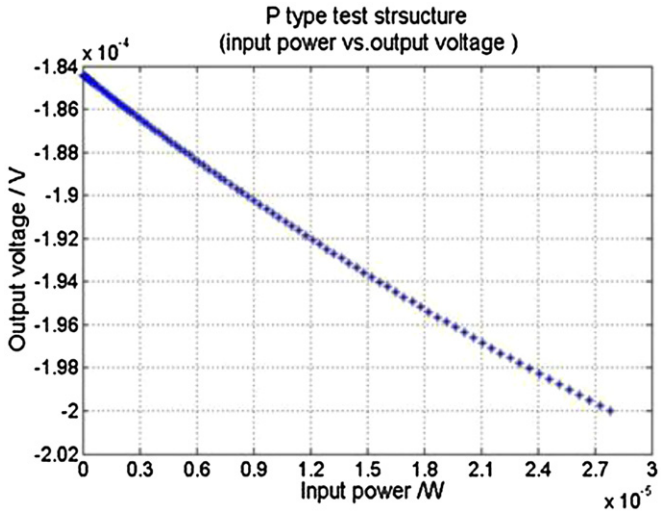

Figure 10. p-type thermopile test structure characterization input power versus output voltage.

in a positive output voltage as the Seebeck coefficient of n-type poly-Si is negative. The input voltage can be converted to input power by

$$P_{\text{in}} = V_{\text{in}}^2 / R_{\text{heater}}. \tag{19}$$

Figure 9 shows the curve of output voltage versus input power and it shows a good linear relationship.

Figure 10 shows the testing results of the p-type single thermocouple. The results are opposite to that of the n-type single thermocouple as the Seebeck coefficient of p-type poly-Si, in this case, is positive.

The measurement to determine the Seebeck coefficient and thermal conductance was conducted in vacuum to eliminate the influence of the conductance from air. The entire measurement was carried out at a pressure lower than 1×10^{-4} mbar.

Table 2. Thermal conductivity and Seebeck coefficient of the n/p-type poly-Si.

	n-type poly-Si	p-type poly-Si
Thermal conductivity (W mK^{-1})	31.9	33.6
Seebeck coefficient (μV K^{-1})	−118	137

In order to get the Seebeck coefficient and thermal conductivity of poly-Si, the temperature coefficients of resistance (TCRs) of the poly-Si are measured by getting different I/V curves for different temperatures first. The results from the measurements show that the TCR of n-type poly-Si and p-type poly-Si are -0.22% K^{-1} and -0.17% K^{-1}, respectively. The temperature of the hot-junction can then be obtained by the *I–V* curve of the thermal sensor shown in figure 6(*b*). With the same method mentioned in [29], the thermal conductance and Seebeck coefficient are calculated. The thermal conductivity of n-type poly-Si and p-type poly-Si are 31.8 W mK^{-1} and 30.7 W mK^{-1}, respectively, and the Seebeck coefficient of n-type poly-Si and p-type poly-Si are -118 μV K^{-1} and 137 μV K^{-1}, respectively. The results are shown in table 2.

3.3. Characterization of the conventional planar thermopile

The micro-heater is placed at the central part of the thermopile sensor (figure 11). A voltage bias was added on the micro-heater to heat it up. The micro-heater performs as a heat source, imitating the infrared source. The semiconductor parameter analyzer equipped with a probe station is utilized to conduct the measurement.

The thermal transfer in the thermopile is different using a micro heater and a real IR source. In order to address the difference, a simulation with ANSYS software was done. A micro heater is added near the hot-junction of the thermopile and heat flux is added onto this heater instead of the whole absorber. The total power added to the thermopile is the same as used in the simulation as discussed in section 2.2. Figure 12 shows the simulation results with the micro heater. The temperature difference between the hot-junction and cold-junction is 1.5499 K while using the microheater and 1.5603 K in case of the IR source. The difference is less than 1% which means that the use of a microheater to imitate the IR source is reasonable.

The measurement results of the n-type conventional coplanar thermopile sensors in atmosphere are shown in figure 13. The voltage bias also varied from -5 to 5 V in steps of 0.1 V. By utilizing equations (3) and (18), we obtained the responsivity of the n-type conventional coplanar thermopile sensors. The derived R_s of the n-type thermopile without vacuum is 31.9 V W^{-1}. The electrical resistance of the n-type thermopile was measured to be 190 kΩ. Then the NEP of the n-type thermopile is derived to be $1.76^{*}10^{-6}$ W without vacuum. The D^{*}, without vacuum, is derived by equations (14) and (15), where the absorption area is $1^{*}10^{5}$ μm^2, and it is 0.58 cm Hz$^{1/2}$ W^{-1}. All parameters R_s, D^{*} and NEP are all shown in table 3.

The measurement results of the p-type coplanar thermopile is shown in figure 14. R_s, NEP and D^{*} are all

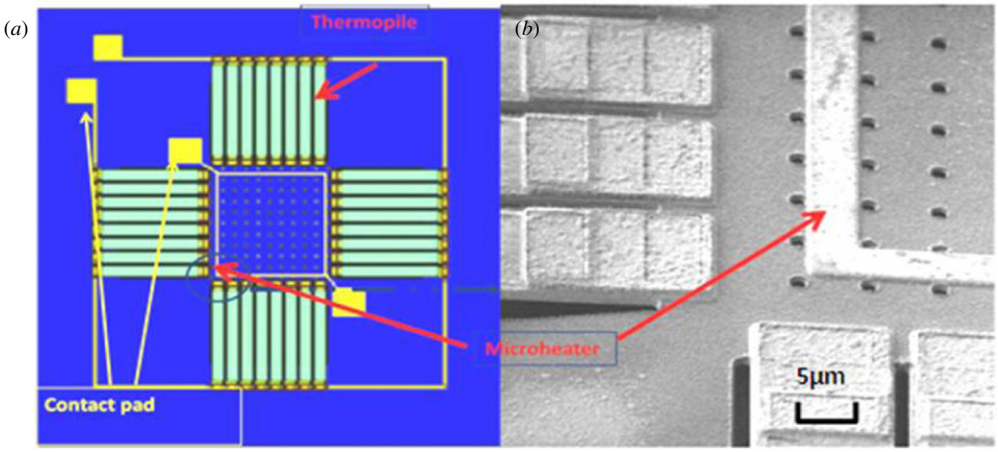

Figure 11. (*a*) Schematic drawing and (*b*) SEM picture of the micro-heater.

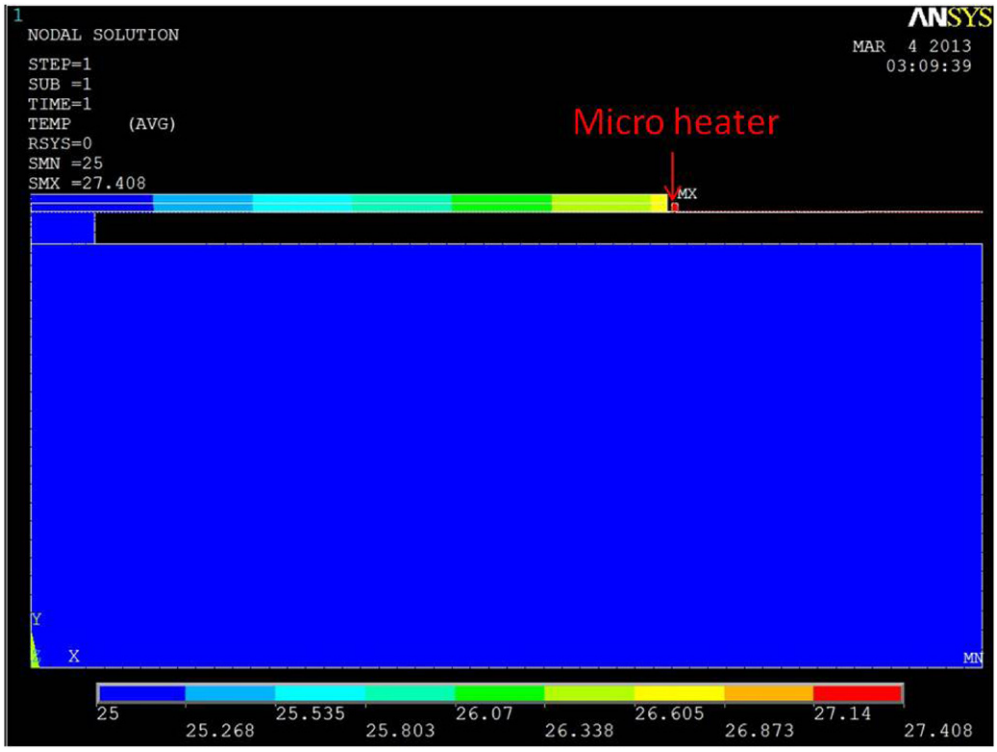

Figure 12. 2D ANSYS simulation results with microheater to show the cross-sectional view of the temperature difference in the thermopile.

measured or derived in the same way as the n-type thermopile. The estimated R_s of the p-type thermopile without vacuum is 30.0 V W^{-1}. The electrical resistance of the p-type thermopile was measured to be 115 kΩ. Then the NEP of the n-type thermopile is derived to be $1.45*10^{-6}$ W without vacuum and the D^* is 0.69 cm $Hz^{1/2}$ W^{-1} with the same value of absorb area. R_s, D^* and NEP of the p-type thermopile are also shown in table 3.

3.4. Characterization of the SDL thermopile

Based on the same way stated in section 4.1, the characterization of the SDL thermopile was conducted. The measurement results without vacuum are shown in figure 15. The output voltages are also proportional to the input power. The measured R_s of the SDL thermopile without vacuum is 88.5 V W^{-1}. The resistance of the SDL thermopile was tested, which is 306 kΩ, to derive the NEP. The NEP of the SDL thermopile is $0.81*10^{-6}$ W without vacuum and D^* is 1.24 cm $Hz^{1/2}$ W^{-1}. R_s, D^* and NEP of the SDL thermopile are also shown in table 3.

Compared to both the coplanar thermopiles, the SDL thermopile has a much better performance. This great advantage lies in mainly two key parameters of the thermopile: low thermal conductance and high Seebeck coefficient difference.

As shown in figure 2, there is no metal connecting the hot-junction and cold-junction in SDL thermopile. The thermal conductances of one single thermocouple in the three kinds of thermopile were calculated based on the measured thermal

Table 3. Performance of the three types of thermopiles.

	SDL thermopile			p-type thermopile			n-type thermopile		
	NEP (10^{-6} W)	D^* (cm $Hz^{1/2}$ W^{-1})	R_s (V W^{-1})	NEP (10^{-6} W)	D^* (cm $Hz^{1/2}$ W^{-1})	R_s (V W^{-1})	NEP (10^{-6} W)	D^* (cm $Hz^{1/2}$ W^{-1})	R_s (V W^{-1})
Atmosphere (assuming emissivity = 1)	0.81	$1.24*10^8$	88.5	1.45	$0.69*10^8$	30.0	1.76	$0.58*10^8$	31.9
Vacuum (assuming emissivity = 1)	0.35	$2.85*10^8$	202.8	0.63	$1.57*10^8$	68.8	0.77	$1.30*10^8$	73.2
Atmosphere (assuming emissivity = 0.8)	0.82	$0.99*10^8$	70.8	1.62	$0.55*10^8$	24.0	1.73	$0.45*10^8$	25.6
Vacuum (assuming emissivity = 0.8)	0.35	$2.28*10^8$	162.3	0.63	$1.26*10^8$	55.1	0.77	$1.04*10^8$	58.6

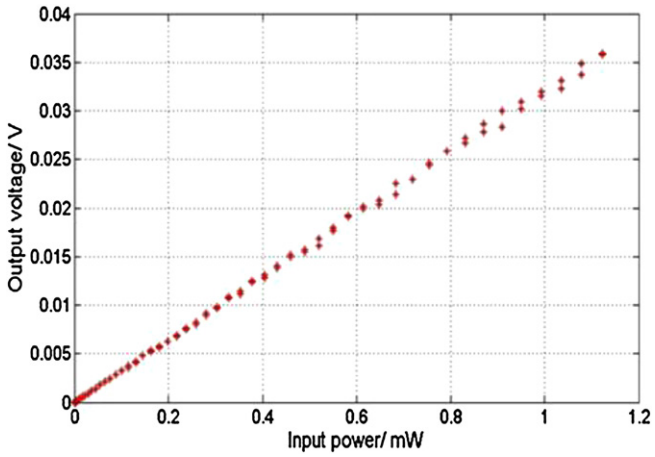

Figure 13. Thermopile sensor characterization input power versus output voltage of the n-type.

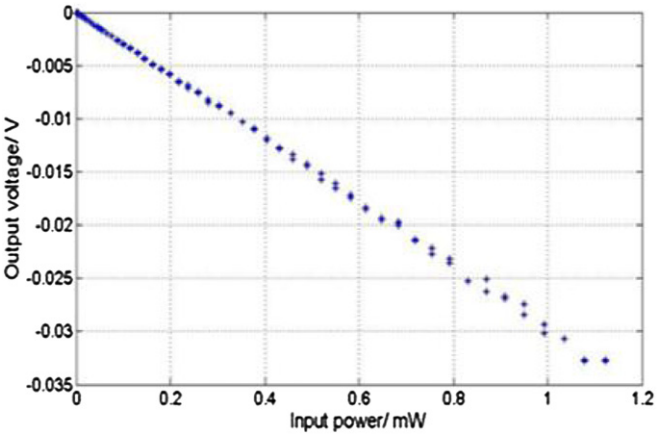

Figure 14. Thermopile sensor characterization input power versus output voltage of the p-type.

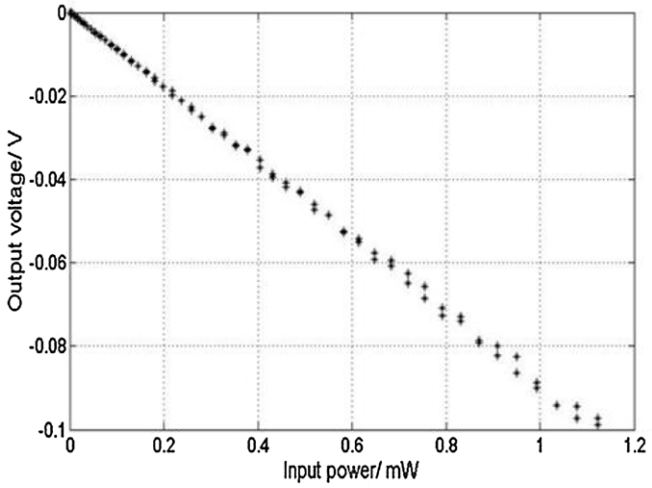

Figure 15. Thermopile sensor input power versus output voltage of the SDL thermopile.

conductance shown in table 2. The thermal conductance of the SDL thermocouple is $0.1385{*}10^{-5}$ W K^{-1} compared with $0.141{*}10^{-5}$ W K^{-1} and $0.147{*}10^{-5}$ W K^{-1} of the n-type thermocouple and p-type thermocouple, respectively.

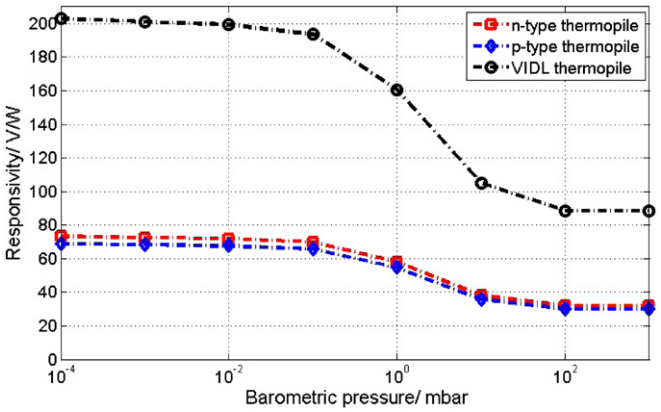

Figure 16. Thermopile characterization under different barometric pressure values.

The thermal conductance of SDL thermocouple is less than the coplanar thermocouples.

Meanwhile, the SDL thermocouple is formed by a pair of n/p-type poly-Si. The Seebeck of n-type poly-Si and p-type poly-Si are -118 μV K^{-1} and 137 μV K^{-1} respectively (table 3), while the Seebeck coefficient of Al is only -1.8 μV K^{-1} (table 1). Therefore the Seebeck coefficient difference of SDL thermocouple is much higher than it of coplanar ones. The calculated Seebeck coefficient difference is 225 μV K^{-1}, compared with 116.2 μV K^{-1} and 138.8 μV K^{-1} of the n-type thermocouple and p-type thermocouple, respectively. The Seebeck coefficient difference of the SDL thermocouple is almost double of that of the coplanar thermocouples.

3.5. Characterization of thermopile in vacuum

Measurement on the three kinds of thermopile was also conducted in different vacuum levels with the probe-station mentioned in previous section equipped with a vacuum chamber. The measurement results are shown in figure 16. From this figure, it can be observed that the influence of the thermal conductance of air is significant. According to equation (9), R_s is proportional to the thermal resistance, which means that R_s is inversely proportional to the thermal conductance. Then the influence of the thermal conductance of air can be calculated. Around 69% of the thermal conductance of the device comes from the air, therefore it is important to reduce the area of the thermopile. The SDL thermopile has the advantage of a smaller footprint compared to the n/p-series coplanar thermopile like those in [4, 22, 26].

With the same poly-Si strips dimensions and the same number of thermocouples, the area of the thermopile legs is doubled while the area of the absorber is quadrupled. According to the dimensions and the number of thermocouples in this paper (600 μm in length, 12 μm in width and 96 thermocouples per thermopile), the area of the n/p-series coplanar thermopile will become almost 2.3 times of the SDL thermopile. Under atmospheric conditions, the total thermal conductance of the SDL thermopile is $0.28{*}10^{-3}$ W K^{-1}, derived from the measured Seebeck coefficient (table 2) and responsivity (R_s) with equations (9)–(13). In the vacuum

chamber, the influence of the atmosphere is limited and the thermal conductance of the SDL thermopile from the structure and radiation can be determined to be $0.12^{*}10^{-3}$ W K^{-1}. This indicates that 56% of the thermal conductance is contributed from the air under atmospheric pressure. Thus, when the area of the coplanar thermopile becomes 2.3 times of the SDL thermopile, then the thermal conductance of the coplanar thermopile from the air, $K_{g\_co-planar}$ becomes 2.3 times of the thermal conductance of the SDL thermopile from the air,K_{g_SDL}, while the area of the cross section of the poly-Si stays the same so we can assume that the thermal conductance from the structure stays also the same, $K_{s\_SDL} = K_{s\_co-planar}$. With this assumption the total thermal conductance of the n/p-series coplanar thermopile will increase to $0.48^{*}10^{-3}$ W K^{-1}, which means that the thermal conductance will increase over 70% compared to the SDL thermopile. Thus the responsivity R_s of the SDL is over 70% larger than that of the n/p-series coplanar thermopile, according to equation (9), showing the great advantage of the SDL thermopile.

4. Conclusion

Using the CMOS-compatible process, design, fabrication and testing of the micromachined n/p-type poly-Si thermopile in both coplanar and SDL configurations have been reported. Both the analytical calculation and experimental data suggest that the SDL thermopile has advantages in terms of the thermal conductance and Seebeck coefficient difference which make the SDL thermopile superior to the conventional coplanar thermopile. Although the resistance of the SDL thermopile is higher than the conventional coplanar thermopile, both the responsivity and detectivity of the SDL thermopile are better. Characterization of the SDL thermopile shows that the responsivity in vacuum and air are up to 202.8 V W^{-1} and 88.5 V W^{-1}, respectively; and the detectivity in vacuum and air are up to $2.85^{*}10^{8}$ cm Hz$^{1/2}$ W^{-1} and $1.24^{*}10^{8}$ cm Hz$^{1/2}$ W^{-1}, respectively.

This new SDL thermopile provides improved sensor performance over the conventional coplanar ones in terms of small footprint and less surface area exposed to air. In applications operated in air, the SDL thermopile is proved to be a superior design.

Acknowledgments

The authors would like to acknowledge the support by SERC Grant Nos 1021650084 from A*STAR, Singapore and NRF Competitive Research Programme R-263-000-A27-281, Singapore.

References

[1] Cole B E, Higashi R E and Wood R A 1998 Monolithic two-dimensional arrays of micromachined microstructures for infrared applications *Proc. IEEE* **86** 1676–86
[2] Wood R A 1993 Uncooled thermal imaging with monolithic silicon focal arrays *Proc. SPIE* **2020** 322–9
[3] Xu D, Xiong B, Wang Y and Li T 2011 Robust array-composite micromachined thermopile IR detector by CMOS technology *IEEE Electron Device Lett.* **32** 1761–3
[4] Wu H, Emadi A, Sarro P M, de Graaf G and Wolffenbuttel R F 2011 A surface micromachined thermopile detector array with an interference-based absorber *J. Micromech. Microeng.* **21** 074009
[5] Du C-H and Lee C 1999 Optimization criteria of CMOS compatible thermopile sensors *Proc. SPIE* **3893** 116–26
[6] Xie J, Lee C, Wang M-F and Tsai J M 2011 Microstructures for characterization of seebeck coefficient of doped polysilicon films *Microsyst. Technol.* **17** 77–83
[7] Leonov V, Torfs T, Fiorini P and Van Hoof C 2007 Thermoelectric converters of human warmth for self-powered wireless sensor nodes *IEEE Sensors J.* **7** 650–7
[8] Xu D, Xiong B and Wang Y 2010 Self-aligned thermoelectric infrared sensors with post-CMOS micromachining *IEEE Electron Device Lett.* **31** 512–4
[9] Kong S H and Wolffenbuttel R F 2005 Spectral performance of a micromachined infrared spectrum analyzer in silicon *IEEE Trans. Instrum. Meas.* **54** 264–7
[10] Xu D, Xiong B and Wang Y 2011 Micromachined thermopile IR detector module with high performance *IEEE Photonics Technol. Lett.* **23** 149–51
[11] Vullers R J M, van Schaijk R, Doms I, Van Hoof C and Mertens R 2009 Micropower energy harvesting *Solid-State Electron.* **53** 684–93
[12] Suman S, Gaitan M, Joshi Y and Harman G G 2005 Wire-bonding process monitoring using thermopile temperature sensor *IEEE Trans. Adv. Packag.* **28** 685–93
[13] Escriba C, Campo E, Esteve D and Fourniols J Y 2005 Complete analytical modeling and analysis of micromachined thermoelectric uncooled IR sensors *Sensors Actuators* A **120** 267–76
[14] Xu D, Xiong B and Wang Y 2010 A high sensitivity CMOS compatible micromachined thermopile IR sensor *Electrochem. Solid-State Lett.* **13** J106–9
[15] Xu D, Jing E, Xiong B and Wang Y 2010 Wafer-level vacuum packaging of micromachined thermoelectric IR sensors *IEEE Trans. Adv. Packag.* **33** 904–11
[16] Lindeberg M, Yousef H, Odjegård H R, Martin H and Hjort K 2008 A PCB-like process for vertically configured thermopiles *J. Micromech. Microeng.* **18** 065021
[17] Xu D, Xiong B, Wu G, Ma Y and Wang Y 2012 Uncooled thermoelectric infrared sensor with advanced micromachining *IEEE Sensors J.* **12** 2014–23
[18] Emadi A, Wua H, Grabarnika S, DeGraaf G, Hedstenb K, Enokssonb P, Correiac J H and Wolffenbuttel R F 2010 Fabrication and characterization of IC-compatible linear variable optical filters with application in a micro-spectrometer *Sensors Actuators* A **162** 400–5
[19] Kong S H, Wijingaards D D L and Wolffenbuttel R F 2001 Infrared micro-spectrometer based on a diffraction grating *Sensors Actuators* A **92** 88–95
[20] de Graaf G, der Vlist W and Wolffenbuttel R F 2008 Design and fabrication steps for a MEMS-based infrared spectrometer using evanescent wave sensing *Sensors Actuators* A **142** 211–6
[21] Yoo K P, Kwon K H, Min N K, Kim S D and Choi W S 2008 A front-side dry-etched thermopile detector with 3–5 μm infrared absorber and its application to novel NDIR CO_2 gas sensors *Proc. IEEE Int. Conf. Sensors (Puglia, Italy)* pp 894–7
[22] Xu D, Xiong B, Wang Y, Liu M and Li T 2009 Integrated micromachined thermopile IR detectors with an XeF2 dry-etching process *J. Micromech. Microeng.* **19** 125003
[23] Park S-C, Yoon S-I, Lee C-i, Kim Y-J and Song S 2009 A micro-thermoelectric gas sensor for detection of hydrogen and atomic oxygen *Analyst* **134** 236–42
[24] Sarro P M 1987 Integrated silicon thermopile infrared detectors *PhD Thesis* Delft Technical University

[25] Lenggenhager R 1994 CMOS thermoelectric infrared sensors *PhD Thesis* ETH Zurich
[26] Xie J, Lee C and Feng H 2010 Design, fabrication, and characterization of CMOS MEMS-based thermoelectric power generators *J. Microelectromech. Syst.* **19** 317–24
[27] Yousef H, Hjort K and Lindeberg M 2007 Vertical thermopiles embedded in a polyimide-based flexible printed circuit board *J. Microelectromech. Syst.* **16** 1341–8
[28] Mattsson C G, Thungstrom G, Bertilsson K, Nilsson H-E and Martin H 2009 Fabrication and characterization of a design optimized SU-8 thermopile with enhanced sensitivity *Meas. Sci. Technol.* **20** 115202
[29] Wang Z, Leonov V, Fiorini P and Van Hoof C 2009 Realization of a wearable miniaturized thermoelectric generator for human body applications *Sensors Actuators* A **156** 95–102
[30] Wang Z, Fiorini P, Leonov V and Van Hoof C 2009 Characterization and optimization of polycrystalline Si70%Ge30% for surface micromachined thermopiles in human body applications *J. Micromech. Microeng.* **19** 094011
[31] Xie J, Lee C, Wang M-F, Liu Y and Feng H 2009 Characterization of heavily doped polysilicon films for CMOS-MEMS thermoelectric power generators *J. Micromech. Microeng.* **19** 125029
[32] Wolffenbuttel R F 1992 Silicon micromachining for integrated radiant sensors *Sensors Actuators* A **30** 109–15
[33] Mattsson C G, Bertilsson K, Thungström G, Nilsson H-E and Martin H 2009 Thermal simulation and design optimization of a thermopile infrared detector with an SU-8 membrane *J. Micromech. Microeng.* **19** 055016
[34] Mattsson C G, Thungström G, Rödjegård H, Bertilsson K, Nilsson H-E and Martin H 2009 Experimental evaluation of a thermopile detector with SU-8 membrane in a carbon dioxide meter setup *IEEE Sensors J.* **9** 1633–8
[35] Mattsson C G, Thungström G, Bertilsson K, Nilsson H-E and Martin H 2008 Design of a micromachined thermopile infrared sensor with a self-supported SU-8 membrane *IEEE Sensors J.* **8** 2044–52
[36] Yoon S-I and Kim Y-J 2010 A flexible tactile sensor based on a thermoelectric device for simultaneous detection of contact heat and contact force *J. Micromech. Microeng.* **20** 105017
[37] Choi Y-H, Kim M-g, Kang D-H, Sim J, Kim J and Kim Y-J 2012 An electrodynamic preconcentrator integrated thermoelectric biosensor chip for continuous monitoring of biochemical process *J. Micromech. Microeng.* **22** 045022
[38] Du C-H and Lee C 2000 3D thermoelectric Structures derived from a new mixed micromachining process *Japan. J. Appl. Phys.* **39** 7125–9
[39] Du C-H and Lee Chengkuo 2002 Characterization of thermopile based on complementary metal-oxide-semiconductor (CMOS) materials and post CMOS micromachining *Japan. J. Appl. Phys.* **41** 4340–5
[40] Xu D, Xiong B and Wang Y 2010 Modeling of front-etched micromachined thermopile IR detector by CMOS technology *J. Microelectromech. Syst.* **19** 1331–40
[41] Xu D, Xiong B and Wang Y 2010 Design, fabrication and characterization of a front-etched micromachined thermopile for IR detection *J. Micromech. Microeng.* **20** 115004
[42] Roncaglia A, Mancarella F and Cardinali G C 2007 CMOS-compatible fabrication of thermopiles with high sensitivity in the 3–5 μm atmospheric window *Sensors Actuators* B **125** 214–23
[43] Du C-H and Lee C 1999 Optimization criteria of CMOS compatible thermopile sensors *SPIE* **3893** 0277–786
[44] Xu D, Xiong B and Wang Y 2010 A CMOS compatible micromachined thermopile IR sensor with high sensitivity *Electrochem. Solid-State Lett.* **13** J106–9
[45] Wu H, Grabarnik S, Emadi A, de Graaf G and Wolffenbuttel R F 2009 Characterization of thermal cross-talk in a MEMS-based thermopile detector array *J. Micromech. Microeng.* **19** 074022
[46] Wu H, Emadi A, Grabarnik S, de Graaf G and Wolffenbuttel R F 2009 Static and dynamic analysis of thermal cross-talk in an thermopile detector array for use in an microspectrometer *Procedia Chem.* **1** 1139–42
[47] Ford J M 1983 Al/Poly Si specific contact resistivity *IEEE Electron Device Lett.* **7** 255–7
[48] Sharpe W N Jr, Pulskamp J, Gianola D S, Eberl C, Polcawich R G and Thompson R J 2006 Strain measurements of silicon dioxide microspecimens by digital imaging processing *Exp. Mech.* **47** 649–58
[49] Proctor S J, Linholm L W and Mazer J A 1983 Direct measurement of interfacial contact resistance, end contact resistance, and interfacial contact layer uniformity *IEEE Trans. Electron Devices* **30** 1535–42